Neurosci. Bull. June, 2022, 38(6):576–590
https://doi.org/10.1007/s12264-022-00838-5

www.neurosci.cn
www.springer.com/12264

ORIGINAL ARTICLE

Whole-Brain Direct Inputs to and Axonal Projections from Excitatory and Inhibitory Neurons in the Mouse Primary Auditory Area

Mengting Zhao[1] · Miao Ren[2] · Tao Jiang[3] · Xueyan Jia[3] · Xiaojun Wang[2] · Anan Li[1,3] · Xiangning Li[1,3] · Qingming Luo[2] · Hui Gong[1,3]

Received: 8 June 2021 / Accepted: 26 December 2021 / Published online: 21 March 2022

Abstract Neurons in the primary auditory area (AUDp) innervate multiple brain regions with long-range projections while receiving informative inputs for diverse functions. However, the brain-wide connections of these neurons have not been comprehensively investigated. Here, we simultaneously applied virus-based anterograde and retrograde tracing, labeled the connections of excitatory and inhibitory neurons in the mouse AUDp, and acquired whole-brain information using a dual-channel fluorescence micro-optical sectioning tomography system. Quantified results showed that the two types of neurons received inputs with similar patterns but sent heterogeneous projections to downstream regions. In the isocortex, functionally different areas consistently sent feedback-dominated projections to these neurons, with concomitant laterally-dominated projections from the sensory and limbic cortices to inhibitory neurons. In subcortical regions, the dorsal and medial parts of the non-lemniscal auditory thalamus (AT) were reciprocally connected to the AUDp, while the ventral part contained the most fibers of passage from the excitatory neurons and barely sent projections back, indicating the regional heterogeneity of the AUDp-AT circuit. Our results reveal details of the whole-brain network and provide new insights for further physiological and functional studies of the AUDp.

Keywords Primary auditory area · Excitatory · Inhibitory · Direct inputs · Axonal projections

Introduction

The primary auditory area (AUDp, AI, or Au1) is a key part of the auditory areas in processing acoustic [1, 2] and other modalities of sensory [3, 4] and non-sensory information [5, 6]. It is also involved in high-level cognitive behaviors, such as prediction, learning, and decision-making [7, 8].

To uncover the circuits underlying functional implementation, early anatomical studies using traditional tracers, such as horseradish peroxidase and biotinylated dextran amine, have revealed that the AUDp is densely innervated by and has efferent projections to both cortical and subcortical regions [9, 10]. However, these traditional techniques cannot distinguish synaptic inputs from extrasynaptic innervation or passage of fibers [11]. Recent studies using optogenetic identification in serial histological sections or virus-based tracers targeting specific regions have provided more precise connections between the AUDp and other anatomical regions, and cortical subnetworks have proven to be vital for multisensory integration [12, 13]. Reciprocal connections with the auditory thalamus (AT) have been well documented in

Mengting Zhao and Miao Ren have contributed equally to this work.

Supplementary Information The online version contains supplementary material available at https://doi.org/10.1007/s12264-022-00838-5.

✉ Hui Gong
huigong@mail.hust.edu.cn

[1] Britton Chance Center for Biomedical Photonics, Wuhan National Laboratory for Optoelectronics, MoE Key Laboratory for Biomedical Photonics, Huazhong University of Science and Technology, Wuhan 430074, China

[2] Key Laboratory of Biomedical Engineering of Hainan Province, School of Biomedical Engineering, Hainan University, Haikou 570228, China

[3] HUST-Suzhou Institute for Brainsmatics, JITRI, Suzhou 215123, China

rodents [14, 15], and descending pathways to the caudateputamen (CP), inferior colliculus (IC), and many other subcortical regions have also been reported [16, 17].

The AUDp contains diverse neuron types that differ in morphology, neurotransmitter type, and connectivity. Among them, ~75% are excitatory and ~20% are inhibitory [18, 19]. Although these two populations are found in one subregion, they differ in their functional roles. One restriction is that excitatory neurons form local and long-range connections, whereas inhibitory interneurons mainly have local connections [20]. In addition, excitatory neurons in the AUDp have broader action potentials (APs) and discharge as regular-spiking units. In contrast, inhibitory interneurons have sharper APs and discharge as fast-spiking units [21]. Furthermore, the stimulus-following ability of fast-spiking units is significantly better than that of regularly-spiking units [22]. To understand the differences in functional roles between excitatory and inhibitory neurons in the AUDp, it is essential to map the whole-brain connectivity with cell-type specificity.

To date, the brain-wide input-output organization of mouse AUDp is still incompletely understood. Relevant studies on this issue have achieved some results. The whole-brain direct inputs to the AUDp have been quantitatively analyzed using modified rabies virus (RV) in C57BL/6J mice [23]. However, the circuits are not specific to cell types. The Allen Mouse Brain Connectivity Atlas [24], using Cre-dependent adeno-associated virus (AAV) tracing combined with Cre driver lines (mice expressing Cre recombinase in specific types of neurons), characterizes the cell-type-specific whole-brain axonal projections of mouse AUDp and many other brain regions, providing a reference database for research. However, a z-sampling interval of 100 μm between coronal images might result in the omission of labeled neurons or discontinuity in axonal projections. Therefore, the precise characterization and systematic analysis of whole-brain input-output circuits with cell-type specificity require a combination of valid tracing strategies, high-resolution whole-brain imaging, and efficient analytical technology.

In this study, we mapped the direct inputs to and axonal projections from excitatory and inhibitory neurons in the mouse AUDp using a virus-based tracing strategy combined with dual-channel fluorescence micro-optical sectioning tomography (dfMOST) [25] to analyze the neural circuits at submicron resolution. In addition, we established pipelines to automatically and quantitatively dissect the brain-wide connections. Our goal was to provide a comprehensive whole-brain cell-type-specific connectivity depiction of mouse AUDp to facilitate the mechanistic investigation of auditory cortical functions.

Materials and Methods

Animals

All surgical and experimental procedures were approved by the Animal Experimentation Ethics Committee of Huazhong University of Science and Technology, and all efforts were made to minimize the number and suffering of experimental animals. *Thy1*-Cre, *CamKII*α-Cre, and *Vgat*-Cre mice were purchased from the Jackson Laboratory (Bar Harbor, ME, USA). All animals were housed under standard conditions of humidity and temperature with a 12/12 h light/dark cycle, and food and water were available *ad libitum*. Adult mice (2–4 months of age) of both sexes were used.

Viral Constructs

All viruses used in this study were customized or commercially provided by BrainVTA Science and Technology Co. (Wuhan, China) and BrainCase Ltd. AAV-DIO-EGFP-TVA (GT) and AAV-DIO-RG were co-packaged at a ratio of 1:2 to generate littermate virus (lAAV-DIO-GT/RG) [26] as AAV helper virus, and EnvA-pseudotyped RV (EnvA-SADΔG-DsRed) was prepared as previously described [27].

Viral Injections

For retrograde and anterograde tracing, 80 nL of AAV helper virus was injected into the target area [AUDp, anterior–posterior (AP)/medial–lateral (ML)/dorsal–ventral (DV) coordinates (mm): −2.46/−4/−2.2] with a microsyringe pump (UMP3 and Micro4, WPI, USA) in either hemisphere. The coordinates of the injection target were determined using the Allen Reference Atlas [28]. Three weeks later, 200 nL of pseudotyped RV was injected into the same area to allow cell-type-specific retrograde tracing. RV was allowed to express for another 7 days before the mice were sacrificed. Samples labeled with inputs or axonal projections were also stained with propidium iodide (PI) to provide cytoarchitectonic information. The surgical and viral injection procedures have been described in detail elsewhere [27].

Histology

Subsequently, deeply anesthetized mice were perfused with 0.01 mol/L PBS (Sigma-Aldrich Inc., St Louis, MO, USA) followed by 4% paraformaldehyde (Sigma-Aldrich Inc.). The brains were excised and post-fixed in paraformaldehyde for 12 h. For whole-brain imaging, the intact brain

was embedded in glycol methacrylate resin (Ted Pella Inc.). The embedding protocol was as described previously [29]. Briefly, each intact brain was rinsed in PBS and dehydrated in a graded ethanol series (50%, 70%, and 95%), then the brains were immersed in a graded glycol methacrylate series. The samples were then impregnated for 3 days and polymerized at 48°C for 24 h.

Imaging and Preprocessing

For whole-brain imaging, the embedded brain samples were imaged by our home-made dfMOST system at a resolution of 0.32 μm × 0.32 μm × 2 μm. Preprocessing, including mosaic stitching and illumination correction, was applied to the acquired two-channel image datasets to produce entire coronal sections. Bilinear resampling and maximum-intensity projection were performed to obtain images with desired resolutions for better visualization and analysis.

Starter Neuron Counting and Infected Volume Assessment

To verify the fidelity of our tracing experiments, we quantified the starter neurons or infected volume for different cases.

For retrograde tracing, the starter neurons were double-positive for enhanced green fluorescent protein (eGFP) and discosoma red fluorescent protein (DsRed) and manually counted using the Cell Counter plug-in in Fiji (https://imagej.nih.gov/ij/) after merging the two channels of images with different pseudo colors to manifest the double-labeled neurons. To check whether the majority of infected neurons were within the scope of the target region, we calculated the proportions of starter neurons in the AUDp and its adjacent regions (the ventral and dorsal auditory areas, i.e. AUDv and AUDd; $n = 4$). The borders of the regions were determined by consulting the Allen Reference Atlas.

For anterograde tracing of excitatory neurons in the AUDp, the dendrites and axons of the neurons were labeled, making it difficult to distinguish infected neurons in the images. In these cases ($n = 3$), we manually segmented the infected volume using Amira software (v6.1.1, FEI) and calculated the proportion of volume contained in the AUDp and its adjacent regions. For anterograde tracing of inhibitory neurons in the AUDp where the starter neurons were distinguishable at the injection site ($n = 3$), we counted them in the same way as described above. The quantified results in both situations were combined to determine the quality of anterograde tracing ($n = 6$).

Data Analysis

Registration

To compare the input and projection patterns of excitatory and inhibitory neurons in the AUDp in different regions of the brain, we registered our data to the Allen Common Coordinate Framework version 3 [30]. The registration method was as previously described [31]. Briefly, the anatomical regions were segmented as landmarks based on the cytoarchitectonic information provided by PI staining or the autofluorescence texture in samples without PI. Then, affine transformation and symmetric image normalization in Advanced Normalization Tools (v2.x) were applied to acquire the transformation parameters. Finally, these transformation parameters were used for neuron centroid registration and high-resolution image registration.

Quantification of Whole-Brain Inputs

Input neurons were automatically detected using NeuroGPS [32] software combined with the TDat [33] format for parallel computation. The programs were written in C++ and run on clusters. Then, the transformation parameters of registration were applied to the centroids of the located somata to map them into a unified space. The numbers of neurons were normalized by dividing the total number in the whole brain to represent the "input strength" for each subregion.

Quantification of Whole-Brain Projections

The axonal filaments were segmented from the images. A Gaussian filter was applied to reduce the noise, followed by a square root transform to remove second-order effects while maintaining high discriminant power in a low signal intensity range. An artificial threshold was set in advance according to the segmentation results of the selected coronal images using a plug-in (Threshold, Otsu) in Fiji. The ultimate segmentation threshold for each coronal slice was a weighted average of the artificial threshold and a threshold automatically generated by the Otsu method [34]. The programs were written in Python 3.6.4 and run on workstations. Artifacts were manually removed in post-processing. The volume of axonal filaments was normalized by dividing the total volume in the whole brain to represent the "projection strength" for each subregion.

Analysis of Input and Projection Strength

Here, we were only concerned about the extrinsic inputs and connections within the gray matter, the neurons and

axonal filaments in the AUDp and within the fiber tracts were identified and included for the visualization but excluded in the strength calculation. Brain regions with a strength <0.003% were neglected.

Visualization and Statistical Analysis

The registered somata and detected volume were loaded into Amira software for three-dimensional (3D) visualization. For statistical analyses, one-way ANOVAs followed by Tukey test if data were normally distributed or the Kruskal-Wallis test if not, were applied to determine statistical differences using GraphPad Prism (v7.00) and SPSS (v26.0.0), with significant differences labeled as $*P < 0.05$, $**P < 0.01$, and $***P < 0.001$. All data values are presented as the mean ± standard error of the mean (SEM).

Results

Mapping Cell-Type-Specific Circuits of Mouse AUDp

To dissect the cell-type-specific connections of mouse AUDp, we injected viral tracers to label the afferent and efferent circuits of excitatory or inhibitory neurons in Cre driver lines. A previously described viral tracing strategy was used to enable comparisons between direct inputs and axonal projections of the AUDp in the same sample (Fig. 1A). Monosynaptic upstream neurons were labeled with DsRed, and efferent axons with eGFP (Fig. 1B). Whole-brain imaging at the mesoscopic scale was performed using the dfMOST system. We acquired >5,000 coronal slices for each brain with a voxel resolution at 0.32 μm × 0.32 μm × 2 μm.

We then quantified the distribution of the starter neurons or the infected volume to check the quality of the retrograde and anterograde tracing (Figs. 1C, S1 and Table S2). Most of the "leaked" starters were in regions adjacent to the AUDp (AUDv and AUDd). Samples with proportions of starter neurons or infected volume <60% inside the AUDp were discarded as heavily contaminated and excluded from our study.

Next, pipelines were established to automatically analyze the connectivity strength between the AUDp and other regions. For anterograde tracing, the axonal filaments were automatically segmented from 2D coronal images (Fig. 1D, upper panel). The segmented volume contained in one subregion was then normalized by the total volume in the whole brain to represent the projection strength from the AUDp to a specific subregion. For retrograde tracing, input neurons were counted automatically using NeuroGPS combined with the TDat format (Fig. 1D, lower panel). Then, the number of neurons in one subregion was divided by the total in the whole brain to represent the input strength from the source region to the AUDp.

Based on the maximum-intensity projection coronal slices of the whole-brain datasets (Figs. S2, S3), we obtained rough connectivity profiles of the excitatory and inhibitory neurons in the AUDp. Both the input connections and axonal projections were mainly ipsilateral, and most of the contralateral connections were within the isocortex. The two types of neurons received inputs from similar upstream regions, among which the isocortex and the thalamus (TH) were the primary sources. However, the projection patterns were different. The axons of labeled excitatory neurons were widely distributed in the isocortex, corpus callosum, CP, TH, and IC and extended far to the hindbrain through the corticospinal tracts. On the contrary, the arbors of inhibitory neurons were mainly scattered in adjacent auditory sub-areas. Thus, whole-brain datasets provided a qualitative view of cell-type-specific neural circuitry. Further quantitative analysis was necessary for obtaining a more detailed and precise connectivity map of mouse AUDp.

Whole-Brain Connectivity Quantification of Mouse AUDp

To understand the connectivity between the AUDp and other brain regions, we first analyzed the 3D distribution of upstream neurons and axonal projections along the AP and ML axes (Fig. 2A). According to the ML distribution, >91% of inputs or projections were ipsilateral; according to the AP distribution, >50% were identified within 1 mm AP, and >77% were within 2 mm AP from the AUDp.

We then mapped the registered somata and volume to the Allen Reference Atlas to provide an intuitive view of the whole-brain circuits (Fig. 2B–D). In general, the two types of neurons in the AUDp shared highly similar upstream regions, including the isocortex, striatum (STR), TH, hippocampal formation (HPF), and hypothalamus (Fig. 2B). Meanwhile, the distribution of axonal projections was heterogeneous (Fig. 2C, D). As noted previously, this was mainly due to morphological differences between the excitatory and inhibitory neurons in the neocortex.

Furthermore, to provide a more precise perception of the circuitry, we analyzed the input/projection strength and identified 111 regions that contained input neurons and/or labeled fibers (Table S3) and further combined them into 53 larger regions to obtain a more general connectivity pattern (Fig. 2E–H). The isocortex was functionally subdivided into four parts (Fig. 2E, G), among which the sensory cortex had ten-times the input/projection strengths of all other cortices.

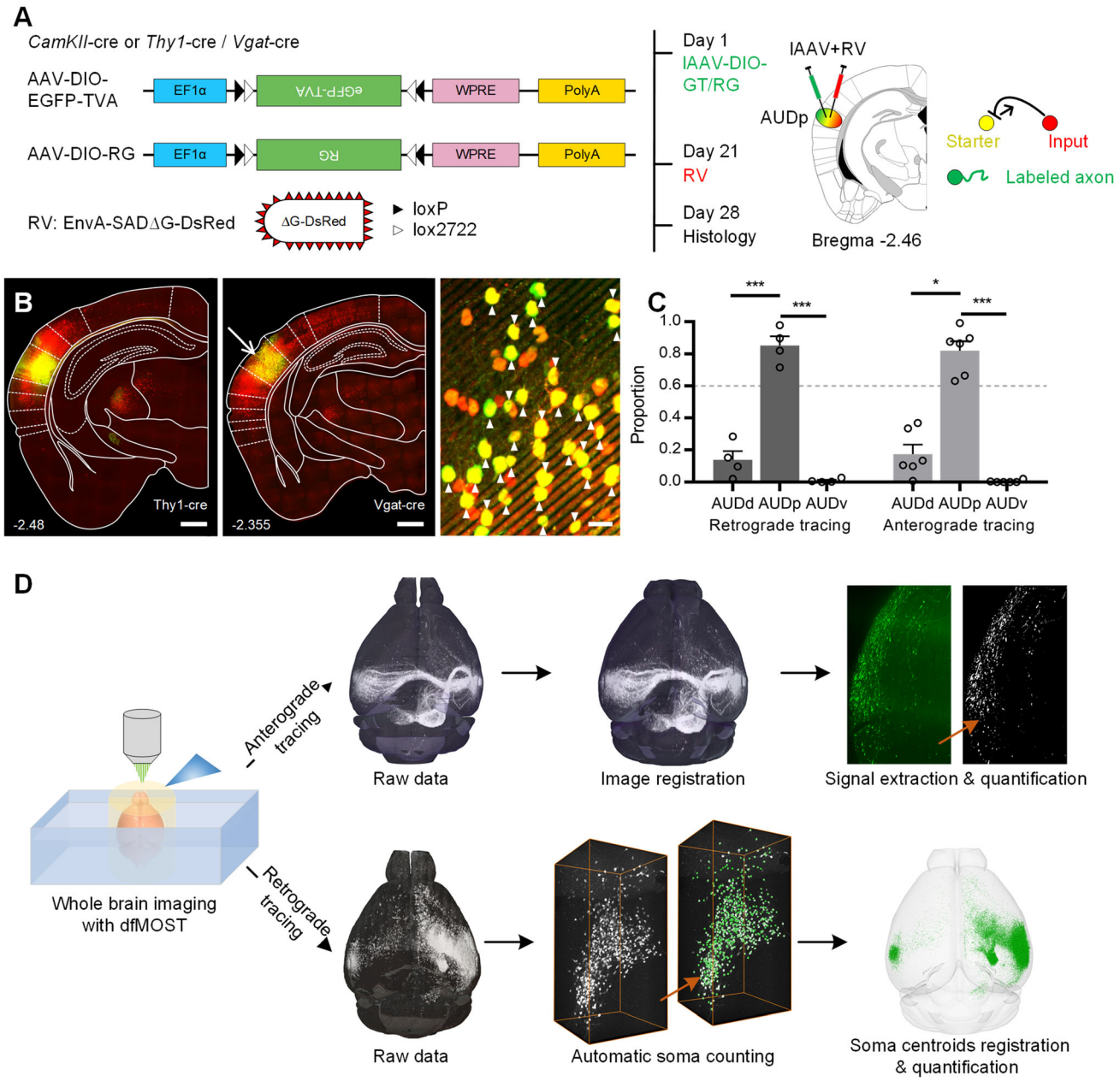

Fig. 1 Experimental procedures for cell-type-specific tracing in the AUDp. **A** Dual-color labeling of retrograde and anterograde tracing with Cre-dependent mice and viral vectors. Left, construction of AAV helper viruses and pseudotyped RV for RV-mediated monosynaptic retrograde and AAV viral anterograde tracing; middle, time course of virus injection and histology for tracing; right, an illustration adapted from the Allen Reference Atlas of the injection site and cartoons of labeled objects. **B** Typical coronal planes of the injection sites for labeling excitatory (left) and inhibitory (middle) neurons as well as an enlarged view of the region indicated by a white arrow in the middle image (right) (lower left, distances from bregma; arrowheads, starter neurons for retrograde tracing; scale bars, left and middle, 500 μm; right, 25 μm). **C** Proportions of starter neurons or infected volume in the AUDp and its adjacent regions (AUDd and AUDv) for retrograde (n = 4) and anterograde (n = 6) tracing (mean ± SEM; $^*P$ <0.05, $^{***}P$ <0.001, one-way ANOVAs followed by Tukey tests if data are normally distributed or Kruskal-Wallis tests if not). **D** Main steps of data acquisition and analysis for anterograde (upper panel) and retrograde (lower panel) tracing.

For regions beyond the isocortex, the TH was the primary source of inputs to the AUDp, followed by the HPF (Fig. 2F). The midbrain (MB) contained the third most numerous inputs to excitatory neurons, but the second least inputs to inhibitory neurons. In all 53 brain regions, three parts of the IC (central ICc, external ICe, and dorsal ICd) were the only regions with significant differences between inputs to excitatory and inhibitory neurons, where direct inputs were observed for excitatory but not for inhibitory neurons in the AUDp. Concerning the axonal

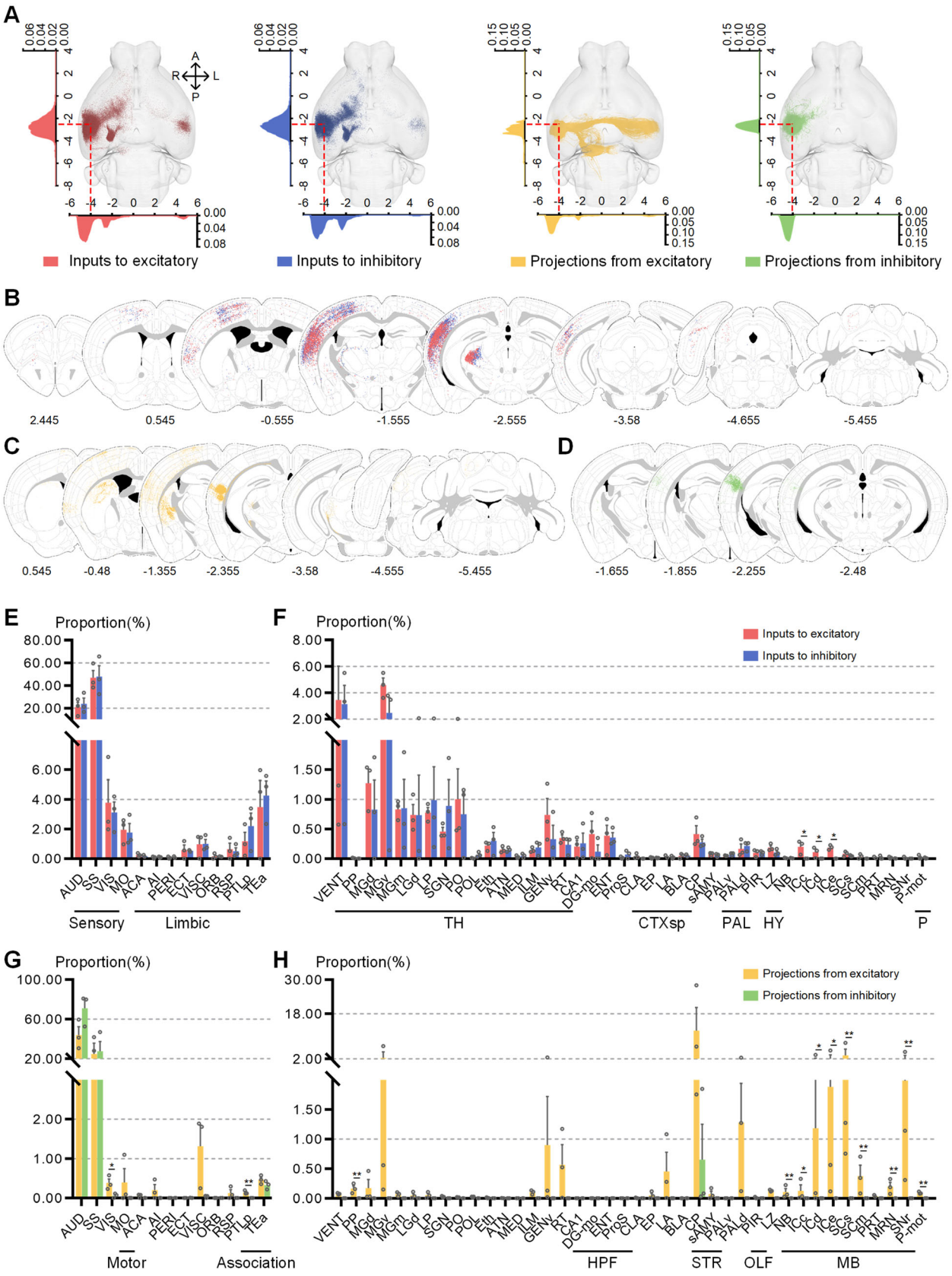
A
Inputs to excitatory
Inputs to inhibitory
Projections from excitatory
Projections from inhibitory
B
2.445
0.545
-0.555
-1.555
-2.555
-3.58
-4.655
-5.455
C
0.545
-0.48
-1.355
-2.355
-3.58
-4.555
-5.455
D
-1.655
-1.855
-2.255
-2.48
E
Proportion(%)
AUD SS VIS MO ACA AI PERI ECT VISC ORB RSP PTLp TEa
Sensory
Limbic
F
Proportion(%)
Inputs to excitatory
Inputs to inhibitory
VENT PP MGd MGv MGm LGd LP SGN PO POL Eth ATN MED ILM GENv RT CA1 DG-mo ENT ProS CLA EP LA BLA CP sAMY PALv PALd PIR LZ NB ICc ICd ICe SCs SCm PRT MRN SNr P-mot
TH
CTXsp
PAL
HY
P
G
Proportion(%)
AUD SS VIS MO ACA AI PERI ECT VISC ORB RSP PTLp TEa
Motor
Association
H
Proportion(%)
Projections from excitatory
Projections from inhibitory
VENT PP MGd MGv MGm LGd LP SGN PO POL Eth ATN MED ILM GENv RT CA1 DG-mo ENT ProS CLA EP LA BLA CP sAMY PALv PALd PIR LZ NB ICc ICd ICe SCs SCm PRT MRN SNr P-mot
HPF
STR
OLF
MB

◀**Fig. 2** Whole-brain connectivity quantification of the AUDp. **A** Three-dimensional visualization of the whole-brain inputs and axonal projections of excitatory or inhibitory neurons in the AUDp. The distribution of inputs or projections along the AP and ML axes is shown on the left and below. The intersection of two red dashed lines indicates the position of the AUDp. **B–D** Representative coronal sections depict inputs (**B**) to the excitatory and inhibitory neurons in the AUDp and axonal projections from the excitatory (**C**) and inhibitory (**D**) neurons in the AUDp, using the same color legends as in (**A**). Numbers indicate the positions of the sections relative to bregma (mm). Each depicted section includes neurons or axons within 50 μm before and after the slice. One dot represents one neuron, and the colored regions indicate the brain areas containing axonal projections. Region outlines with a white background are adapted from the Allen Reference Atlas. **E–H** Quantitative analysis of inputs/projections of the isocortex (**E**, **G**) and regions beyond the isocortex (**F**, **H**). Values for each region are given as the percentage of total direct input neurons or total axonal projection volume in the whole brain. Data are shown as mean ± SEM, $n = 3$ mice per condition. $^{*}P < 0.05$, $^{**}P < 0.01$, $^{***}P < 0.001$, one-way ANOVAs followed by Tukey tests if data were normally distributed or Kruskal-Wallis tests if not. Details of the abbreviations for brain regions and anatomical hierarches are shown in Table S1.

projections from the AUDp to regions beyond the isocortex, the STR, MB, and TH contained the most projections from the excitatory neurons, followed by the pallidum and cortical subplate (Fig. 2H).

In addition, we analyzed the distributions of inputs/projections in the ipsilateral and contralateral hemispheres (Fig. S4). Most of the regions in the isocortex, with several exceptions in the sensory (mouth region of the primary somatosensory, posteromedial visual, and gustatory areas) and limbic (ventral anterior cingulate, ventral agranular insular, and ectorhinal areas) cortices, containing ipsilateral inputs to or projections from the excitatory neurons, were also contralaterally labeled, although the proportions were much lower (by about an order of magnitude). In contrast, the regions beyond the isocortex tended to form only ipsilateral connections with the AUDp. Specifically, no contralateral connections were observed in the TH, and the entorhinal area (ENT) was the only region in the HPF with contralateral inputs to the AUDp.

Cooperativity and Bias Analysis of Whole-Brain Circuits

According to our analysis, the connections were largely reciprocal for excitatory neurons, and the upstream regions usually sent inputs to both types of neurons. Therefore, we further investigated the cooperativity (using Pearson's correlation coefficient, r) and bias (above or below diagonals) between inputs and axonal projections of one population of neurons in the AUDp or between the two populations of either inputs or projections (Fig. 3).

First, we assessed the cooperativity between inputs to excitatory and inhibitory neurons and found high correlations for both the isocortex and other regions (Fig. 3A, E). The regions in the isocortex were close to the diagonal of the scatter diagram, which meant that these regions sent nearly equal inputs to the two types of neurons (Fig. 3A). Other regions showed a slightly lower correlation, with significant differences in the ICc, ICd, and ICe (Fig. 3E). These findings demonstrated that the whole-brain inputs to the two types of neurons are highly cooperative and unbiased.

We then evaluated the cooperativity between axonal projections from the two populations to the isocortex and found a correlation as high as for the inputs to them (Fig. 3B), indicating that the regions containing more projections from one type of neuron contained more from the other. The AUDd was the only region in the isocortex with a significantly higher proportion of fibers from the inhibitory neurons than the excitatory neurons, as most of the inhibitory axonal projections were confined to the auditory areas.

Furthermore, we evaluated the reciprocity bias of connectivity for each type of neurons (Fig. 3C, D, and F). For both types of neurons, the input and projection strengths were significantly correlated for regions in the isocortex (Fig. 3C, D), indicating that the regions in the isocortex that gave more inputs also contained more axonal projections from the AUDp. However, the regions beyond the isocortex rarely formed homologous reciprocal projections (Fig. 3F). It is worth noting that the regions with significant differences between the input/projection strengths were mainly in the MB (the compact part of substantia nigra, cuneiform nucleus and lateral terminal nucleus of the accessory optic tract) and HPF (Ammon's horn, ENT and molecular layer of dentate gyrus). The former were projection-biased, which mainly received top-down inputs from the cortex, and the latter were input-biased, which sent bottom-up information to higher levels. However, since axonal terminals cannot be distinguished from fibers of passage in our quantitative analysis, the conclusions on reciprocal connections between the AUDp and other brain regions need further studies.

Feedback-Dominated Projections from the Isocortex

The isocortex was widely connected with the AUDp as the major input source and projection target (Fig. 2E, G). Next, we investigated the laminar organization of the cortico-cortical connections. Representative coronal images showed the upstream neurons and projecting axons with different layer distribution patterns in the isocortex (Fig. 4A). However, it is still unknown whether there are criteria for these laminar distributions and whether these

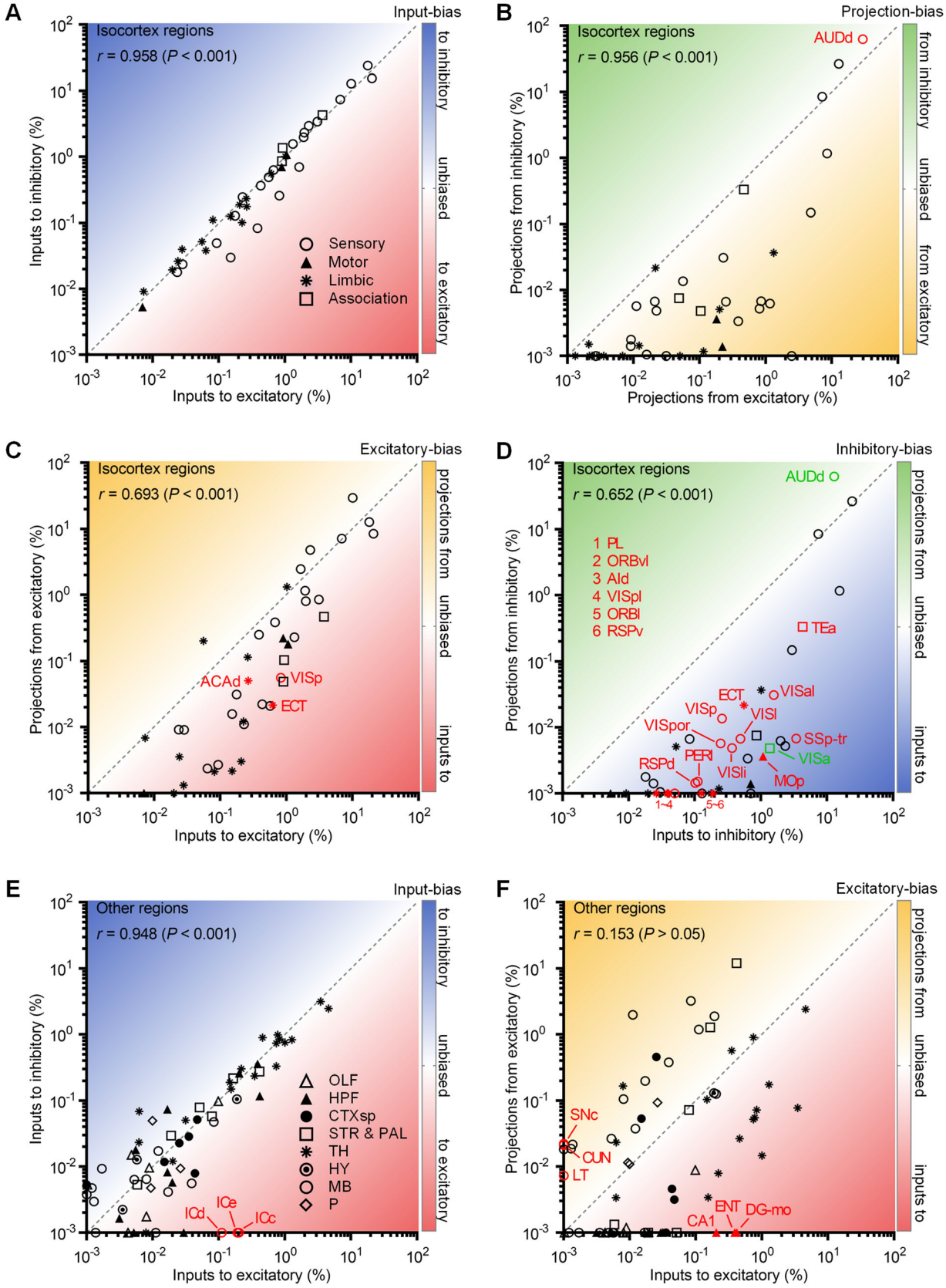
A
Input-bias
Isocortex regions
r = 0.958 (P < 0.001)
Inputs to inhibitory (%)
Inputs to excitatory (%)
to inhibitory
unbiased
to excitatory
Sensory
Motor
Limbic
Association
B
Projection-bias
Isocortex regions
r = 0.956 (P < 0.001)
AUDd
Projections from inhibitory (%)
Projections from excitatory (%)
from inhibitory
unbiased
from excitatory
C
Excitatory-bias
Isocortex regions
r = 0.693 (P < 0.001)
Projections from excitatory (%)
Inputs to excitatory (%)
projections from
unbiased
inputs to
ACAd
VISp
ECT
D
Inhibitory-bias
Isocortex regions
r = 0.652 (P < 0.001)
AUDd
1 PL
2 ORBvl
3 AId
4 VISpl
5 ORBl
6 RSPv
TEa
ECT
VISal
VISp
VISl
VISpor
SSp-tr
VISa
PERI
RSPd
VISli
MOp
1~4
5~6
Projections from inhibitory (%)
Inputs to inhibitory (%)
projections from
unbiased
inputs to
E
Input-bias
Other regions
r = 0.948 (P < 0.001)
Inputs to inhibitory (%)
Inputs to excitatory (%)
to inhibitory
unbiased
to excitatory
OLF
HPF
CTXsp
STR & PAL
TH
HY
MB
P
ICd
ICe
ICc
F
Excitatory-bias
Other regions
r = 0.153 (P > 0.05)
Projections from excitatory (%)
Inputs to excitatory (%)
projections from
unbiased
inputs to
SNc
CUN
LT
ENT
DG-mo
CA1

◀**Fig. 3** Cooperativity and bias analysis of cell-type-specific inputs and projections. **A** Comparison of isocortex inputs to excitatory and inhibitory neurons in the AUDp. **B** Comparison of isocortex projections from excitatory and inhibitory neurons in the AUDp. **C** Comparison of isocortex inputs to and projections from excitatory neurons in the AUDp. **D** Comparison of isocortex inputs to and projections from inhibitory neurons in the AUDp. **E** Comparison of inputs beyond the isocortex to excitatory and inhibitory neurons in the AUDp. **F** Comparison of inputs beyond the isocortex to and projections beyond the isocortex from excitatory neurons in the AUDp. The Pearson product-moment correlation coefficient (r) represents the similarity of the connections between the brain regions and the AUDp. Regions containing an input or projection strength <0.003% for one variable but higher for the other are set on the axis of the latter. Red, P <0.05; green, P <0.01; black P >0.05, one-way ANOVAs followed by Tukey tests if data are normally distributed or Kruskal-Wallis tests if not. Details of the abbreviations for brain regions and anatomical hierarchies are shown in Table S1.

criteria are similar or different across all parts of the isocortex. Therefore, the isocortex was functionally divided into five parts (Fig. 4B) to evaluate the directional features of the cortico-cortical connections as feedforward-dominated (axons terminate in granular layer IV and usually originate in supragranular layers I–II/III), feedback-dominated (terminate outside the granular layer and originate in infragranular layers V–VI), or lateral-dominated (terminate across all layers and originate equally in infragranular and supragranular layers) [35, 36]. The sensory cortex, which contained most of the cortico-cortical connections, was further separated into the auditory cortex and the other sensory cortices (Fig. 4C). The association cortex contained the second most inputs to both types and the third most projections from the excitatory neurons (the second most was the limbic cortex). Overall, the infragranular layers contained the most inputs to both types of neurons and axonal projections from the excitatory neurons compared with the supragranular and granular layers (Fig. 4D).

For input circuits (Fig. 4E, F), the infragranular layers contained more inputs than the supragranular layers and the granular layer for both types of neurons. No significant difference was found between the supragranular layers and the granular layer for inputs to excitatory neurons, but was found between inputs to inhibitory neurons in the other sensory and limbic cortex. Therefore, we deduced that the afferent pathways from different parts of the isocortex to both types of neurons in the AUDp were generally feedback-dominated, with concomitant lateral-dominated projections from the sensory and limbic cortices to inhibitory neurons. For output circuits (Fig. 4G, H), we asked whether the axonal projections in the supragranular layers were significantly more than those in the other layers (suggesting that they were feedback-dominated) or whether the axonal projections in the granular layer were significantly less than those in the other layers (suggesting no feedforward domination). Our results demonstrated that the excitatory and inhibitory neurons sent feedback-dominated projections to the association cortex and the other sensory cortex, respectively. However, the axonal projections comprised both fibers of passage and axonal terminals, and only the latter made real connections between the cortical regions. Further studies are needed to verify our conclusions regarding the directionality of efferent projections from the AUDp.

Taken together, we found that functionally different cortical regions were characterized by specific laminar distributions of connections with specific types of neuron in the AUDp.

AUDp-AT Circuits with Regional Heterogeneity

It is well established that acoustic information usually passes through five subcortical levels [cochlear nuclei, superior olivary complex, nucleus of the lateral lemniscus, IC, and medial geniculate complex (MG)] before reaching the auditory cortex [37]. Here, we focused on the MG and expanded it to the whole AT to obtain a more comprehensive perception of the central auditory system (Fig. 5A). Previous studies have divided the AT into two parts, lemniscal and non-lemniscal, based on their segregated anatomical locations, different connections, and distinct functions [38]. The lemniscal AT indicates the ventral part of the MG (MGv). The non-lemniscal AT surrounds the MGv and can be further divided into three parts: the dorsal part, consisting of the dorsal MG (MGd) and the suprageniculate nucleus (SGN); the medial part MGm; and the ventral part, consisting of the posterior intralaminar thalamic nucleus (PIL) and the peripeduncular nucleus (PP) [15]. Details of the abbreviations and anatomical hierarchies of the AT are listed in Table S4.

Among all subcortical regions that form connections with the AUDp, the TH contained the most inputs to both types of neurons and the second most projections from the excitatory neurons, in which approximately half of these thalamocortical/corticothalamic connections were within the AT (Fig. 2F, H). The MGv was the main area reciprocally connected to the excitatory neurons in the AUDp (Fig. 5B, upper panel). The inputs to inhibitory neurons were densely distributed in both the MGv and several parts of the non-lemniscal AT (Fig. 5B, lower panel). The connectivity profiles across subdivisions of the non-lemniscal AT with the AUDp were heterogeneous (Fig. 5C). In contrast to the MGd/SGN and MGm, which were reciprocally connected to the AUDp, the PIL/PP contained the most projections from the excitatory neurons but barely sent inputs to the AUDp. The axonal projections in the PIL/PP were mostly thick, smooth, and fasciculate,

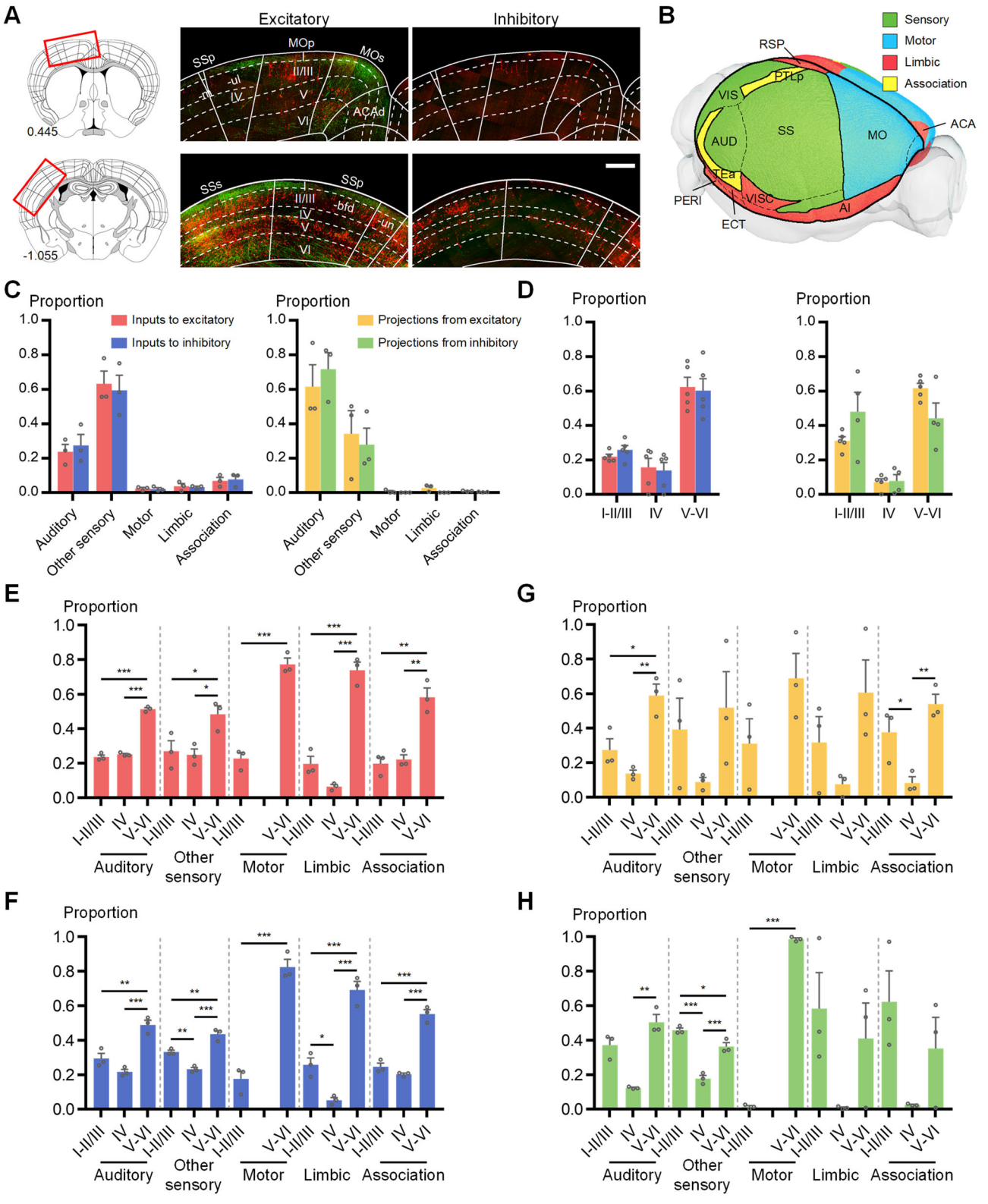
A
Excitatory
Inhibitory
0.445
-1.055
MOp
MOs
SSp
SSs
ACAd
bfd
un
ul
II/III
IV
V
VI
B
Sensory
Motor
Limbic
Association
RSP
PTLp
VIS
SS
MO
ACA
AUD
TEa
PERI
VISC
AI
ECT
C
Proportion
Inputs to excitatory
Inputs to inhibitory
Projections from excitatory
Projections from inhibitory
Auditory
Other sensory
Motor
Limbic
Association
D
I-II/III
IV
V-VI
E
F
G
H

◀**Fig. 4** AUDp-isocortex connections. **A** Coronal views adapted from the Allen Reference Atlas and corresponding images showing cortical areas that contain inputs to (DsRed-labeled neurons) and projections from (eGFP-labeled axons) the excitatory and inhibitory neurons in the AUDp. Maximum-intensity projection at 100 μm. Scale bar, 200 μm. The demarcations and annotations of the brain regions are based on the Allen Reference Atlas after data registration. **B** A three-dimensional view of mouse isocortex from the Allen Reference Atlas showing the anatomical locations of functionally different cortical areas. **C** Quantification of inputs and projections in functionally different cortical regions. **D** Laminar distribution of inputs and projections in five parts of the isocortex. Data are shown as mean ± SEM. I–II/III, supragranular layers; IV, granular layer; V–VI, infragranular layers. **E**–**H** Laminar distribution of inputs to excitatory neurons (**E**), inputs to inhibitory neurons (**F**), projections from excitatory neurons (**G**), and projections from inhibitory neurons (**H**) in five functionally different cortices (**P* <0.05, ***P* <0.01, ****P* <0.001, one-way ANOVAs followed by Tukey tests if data were normally distributed or Kruskal-Wallis tests if not).

indicating that they were mainly fibers of passage (Fig. S5A), while in the MGv, MGm, and MGd/SGN, the axons were diffuse with numerous varicosities, indicating that they were more likely to be axonal terminations forming synaptic connections with the AUDp. These findings demonstrated the distinct connectivity patterns across different parts of the non-lemniscal AT with the AUDp, providing anatomical clues for further functional investigations.

Thus, we summarized the AUDp-AT circuits in mice and created a comprehensive model for the central auditory system (Fig. 5D). Based on previous studies, we amended the thalamocortical projections by targeting both types of neuron in the AUDp, and the PIL/PP contributed little to the reciprocal connections between the non-lemniscal AT and the AUDp.

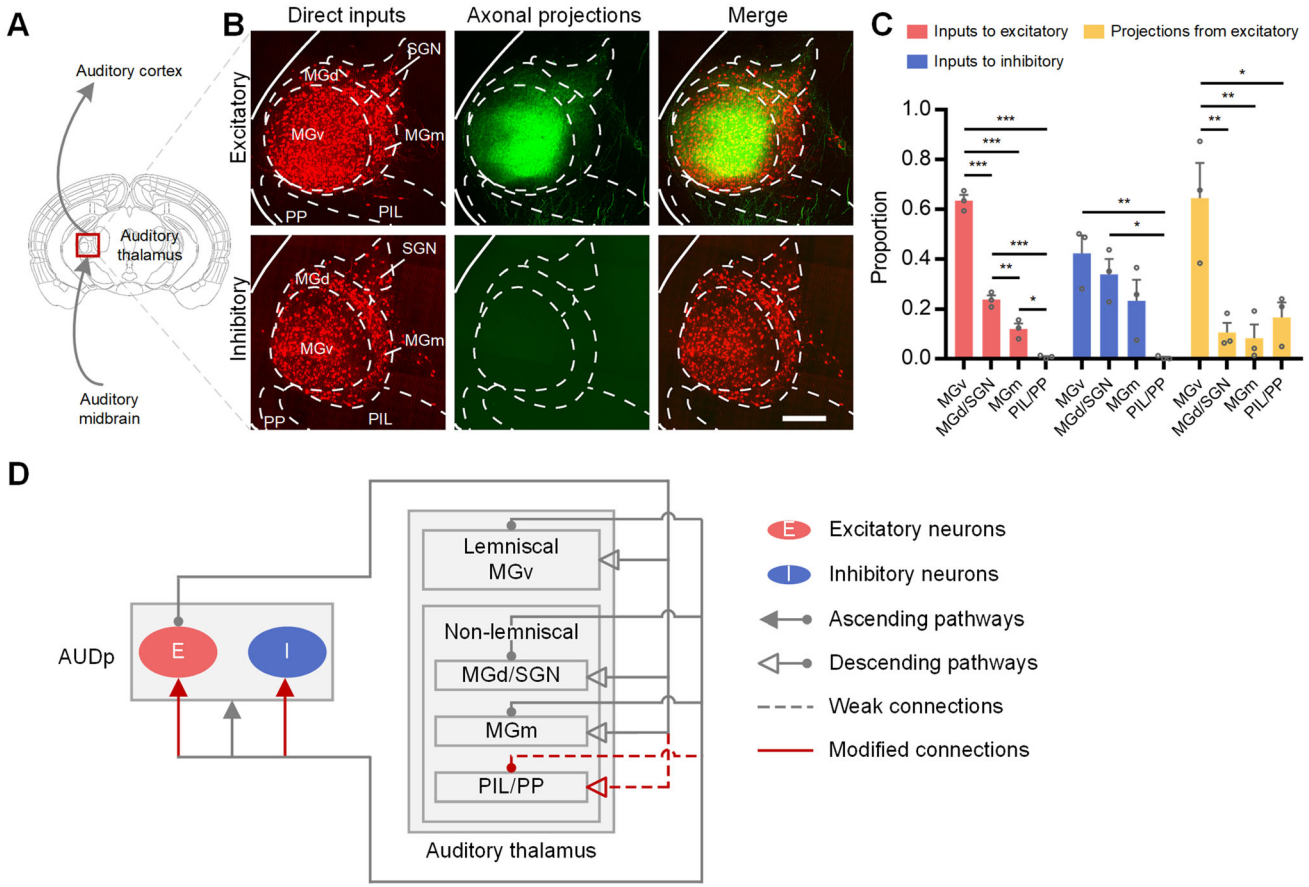

Fig. 5 Central auditory system connections. **A** The central auditory ascending pathway between the auditory midbrain and the auditory cortex for the processing of acoustic information. One of the main subcortical levels, the auditory thalamus (AT), is highlighted in red. The demarcations and annotations of brain regions are based on the Allen Reference Atlas. **B** Representative sections showing the AT with inputs to (DsRed-labeled neurons) and projections from (eGFP-labeled axons) the excitatory (upper panel) and inhibitory (lower panel) neurons in the AUDp, scale bar, 200 μm. **C** Quantification of connectivity between the AT and AUDp (**P* <0.05, ***P* <0.01, ****P* <0.001, one-way ANOVAs followed by Tukey tests if data are normally distributed or Kruskal-Wallis tests if not). **D** Refined connectivity model of the AUDp-AT circuits (red lines, new findings; dashed lines, weak connections). Details of the abbreviations and anatomical hierarchies of the AT are shown in Table S4.

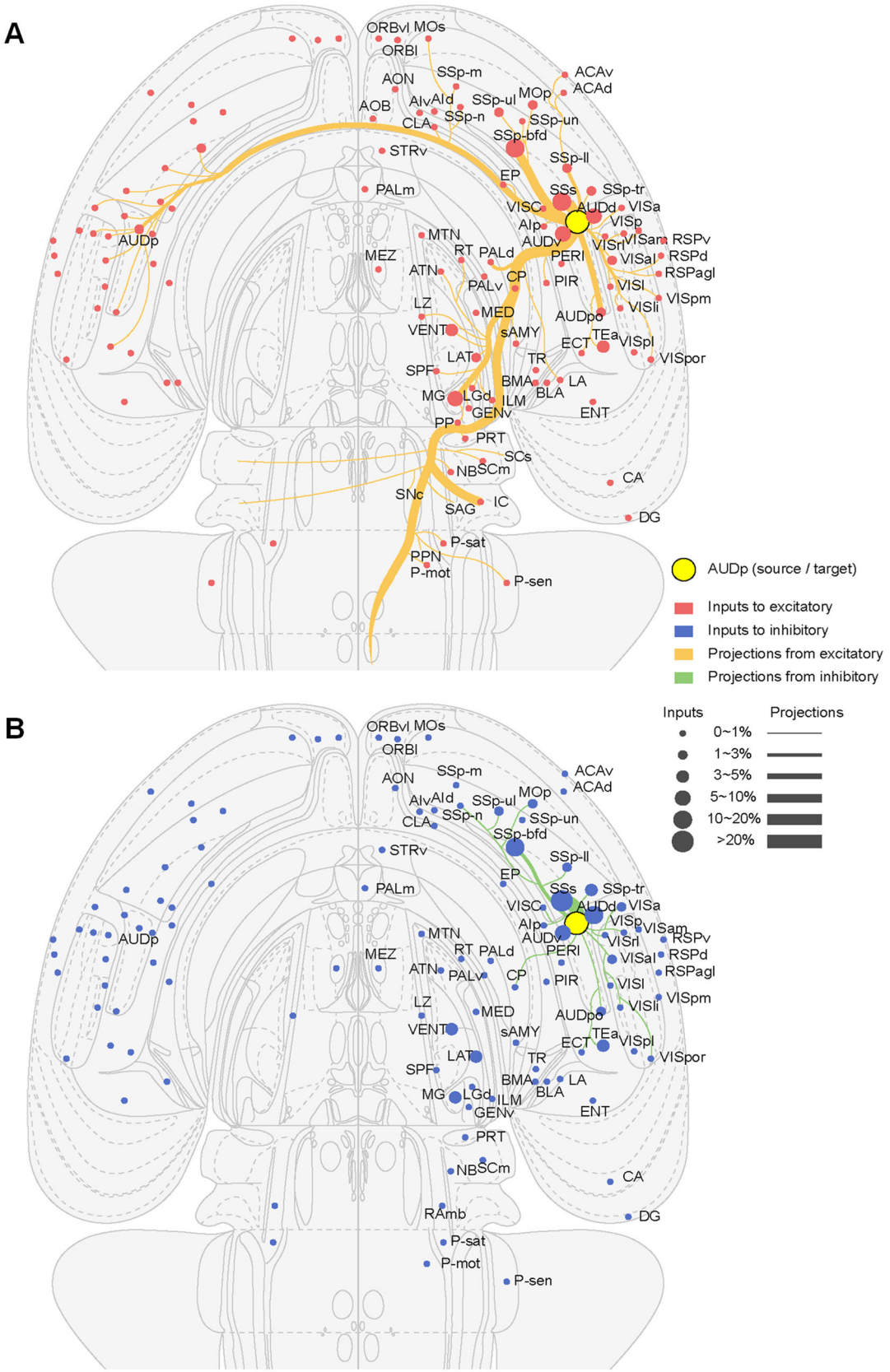
A
ORBvl
MOs
ORBl
AON
SSp-m
ACAv
ACAd
MOp
AOB
AIv
AId
SSp-ul
SSp-n
CLA
SSp-un
SSp-bfd
STRv
SSp-ll
EP
PALm
SSs
SSp-tr
VISC
AUDd
VISa
AIp
VISp
AUDp
MTN
AUDv
VISrl
VISam
RSPv
MEZ
RT
PALd
PERI
VISal
RSPd
ATN
CP
PIR
RSPagl
PALv
VISl
LZ
VISpm
MED
VISli
AUDpo
VENT
sAMY
TEa
ECT
VISpl
LAT
TR
VISpor
SPF
BMA
LA
MG
LGd
ILM
BLA
GENv
ENT
PP
PRT
SCs
NB
SCm
CA
SNc
SAG
IC
DG
P-sat
PPN
P-mot
P-sen
AUDp (source / target)
Inputs to excitatory
Inputs to inhibitory
Projections from excitatory
Projections from inhibitory
B
Inputs
Projections
0~1%
1~3%
3~5%
5~10%
10~20%
>20%
RAmb

◀**Fig. 6** Whole-brain neural circuits of excitatory (**A**) and inhibitory (**B**) neurons in mouse AUDp. Inputs are shown as circles with different diameters, and projections are shown as lines with different widths. Regions with input and projection strengths <0.003% are not shown. Illustrations are adapted from open-access brain atlas templates [50]. The demarcations and annotations of brain regions are based on the Allen Reference Atlas.

Discussion

Audition is vital for animal survival in a dynamic environment; completely uncovering the neural structure of the auditory system is important for understanding the intricate mechanism of the auditory sense. In this study, by combining virus tracing in transgenic mice and the dfMOST system, we comprehensively and selectively labeled the brain-wide connections at mesoscale resolution and automatically generated a description of the whole-brain direct inputs to and axonal projections from excitatory and inhibitory neurons in mouse AUDp.

Overall, the connections between the AUDp and other regions were primarily ipsilateral, which is a common property of the circuits in the cortical regions of rodents [10, 39, 40]. Quantitative analysis showed that the upstream regions sent comparable inputs to excitatory and inhibitory neurons in the AUDp (Fig. 2). Many studies have reported that different types of neuron in one brain region share similar presynaptic partners in the whole brain [27, 39, 41], suggesting convergent external innervation for a given region regardless of cell-type specificity. In contrast, projection patterns are usually cell-type dependent [24].

Cooperativity and bias analysis further revealed that regions presented high cooperativity between the two types of neurons for direct inputs to or axonal projections from the AUDp. However, when focusing on one population of neurons, the inputs and projections were often uncooperative, especially in subcortical regions, suggesting global non-reciprocal connections between subcortical regions and the AUDp.

Furthermore, we compared the laminar distributions of cortico-cortical connections with the AUDp, and deduced that the cortical regions mainly sent feedback-dominated afferents. Meanwhile, the sensory and limbic cortices concomitantly sent lateral-dominated projections to the inhibitory neurons. This is partially consistent with a mapping study of the direct inputs to the AUDp in wild-type mice [23], in which lateral-dominated projections are common. This difference may reflect the different emphases of the two studies; while Costa *et al.* evaluated the cortico-cortical connections by calculating the fraction of labeled neurons within layers I–IV [supragranular layer neurons (SLN)], and defined the feedback-dominated projections as SLN <0.33 and the lateral-dominated as $0.33 < \text{SLN} < 0.66$, our study compared the fractions of input neurons in layers I–II/III and V–VI to measure the significant differences of inputs between the supragranular and the infragranular layers. In addition, labeling specific types of neuron *vs* non-specificity of tracing may also contribute to this difference. However, it should be noted that the directionality of the connections discussed in our study is confined to cortico-cortical projections. The definition of feedforward and feedback rules can be different when considering projections between the cortex and subcortical regions [42].

In the AT, statistical analysis showed that the MGv contained significantly more inputs and projections than the non-lemniscal AT (Fig. 5C), consistent with the well-documented conclusion that the MGv primarily forms reciprocal connections with the AUDp [43, 44]. In the non-lemniscal AT, the PIL/PP contained the most labeled fibers from the excitatory neurons and barely sent inputs to the AUDp, suggesting weak connections between the two regions. Cai *et al.* reported that the PIL/PP mainly innervate the association cortex, while the MGd/SGN and MGm are predominantly connected to the sensory processing centers [15], which is consistent with our findings.

There are several caveats in the interpretation of our tracing results. First, we used *Thy1*-Cre and *CamKIIα*-Cre mice to analyze the connectivity of the excitatory neurons. When comparing the input and projection strengths in 53 regions (Fig. 2), we found no significant differences among them (one-way ANOVAs followed by Tukey's tests). Second, benefitting from our tracing strategy, which enhanced the brightness of axonal projections [26], neurons with long-range axonal projections were observed in anterograde tracing on the inhibitory neurons (Fig. S6), presenting an inhibitory corticostriatal pathway from the AUDp to the dorsal part of the striatum (i.e. CP). These findings provide evidence for long-range corticostriatal inhibitory neurons [16, 45–47], but additional confirmation experiments are needed. Third, a major limitation of our anterograde tracing strategy is that we could not distinguish all the axonal terminals from labeled fibers. Therefore, the output from the AUDp was quantified as the overall number of eGFP-positive pixels within each brain region. Further studies using synaptic markers such as AAV-DIO-mRuby-T2A-synaptophysin-eGFP [48] could overcome this limitation. Fourth, in our study, input neurons in the IC were observed by retrograde tracing on excitatory neurons in the AUDp (Fig. S5B). However, such direct ascending projections from the IC to the AUDp have not yet been formally described [17, 36, 49]. We injected AAV anterograde tracing virus (AAV-CAG-EGFP-WEPR-PA) into the IC of wild-type mice and captured coronal images with a confocal microscope, but did not observe projecting

axons or axonal terminals in the AUDp. We conjectured that this might be due to the weakness of these connections as we only found tens to hundreds of retrogradely labeled neurons in the IC. Meanwhile, the tracing strategy used in our study at a resolution of 0.32 μm × 0.32 μm × 2 μm remarkably enhanced the tracing efficiency across the whole brain. Further systematic confirmation experiments using more sophisticated technology are needed. Finally, the conclusions regarding the neural network of the AUDp would be more credible and precise if the boundaries of the AUDp in this study were defined functionally.

Based on the analysis above, we generated a whole-brain connectivity atlas of excitatory and inhibitory neurons in mouse AUDp (Fig. 6). In summary, the circuitry structures at the level of specific cell types within the AUDp were investigated. The findings reveal many details of the circuitry of the AUDp and can provide new insights for further study into the physiological functions of the auditory areas in mice.

Acknowledgements We thank Peilin Zhao, Qingtao Sun, Zhengchao Xu, Hong Ni, and Zhiwen Xie for help with experiments and data analysis and for constructive comments. We thank the members of the MOST group of Britton Chance Center for Biomedical Photonics and HUST-Suzhou Institute for Brainsmatics for help with experiments and data acquisition. This work was supported by the National Natural Science Foundation of China (61890953, 61890954, and 31871088) and the CAMS Innovation Fund for Medical Sciences (2019–I2M–5–014).

Conflict of interest All authors claim that there are no conflicts of interest.

References

1. Bendor D, Wang XQ. Differential neural coding of acoustic flutter within primate auditory cortex. Nat Neurosci 2007, 10: 763–771.
2. Kaur S, Rose HJ, Lazar R, Liang K, Metherate R. Spectral integration in primary auditory cortex: Laminar processing of afferent input, *in vivo* and *in vitro*. Neuroscience 2005, 134: 1033–1045.
3. Bizley JK, Nodal FR, Bajo VM, Nelken I, King AJ. Physiological and anatomical evidence for multisensory interactions in auditory cortex. Cereb Cortex 2007, 17: 2172–2189.
4. Lakatos P, Chen CM, O'Connell MN, Mills A, Schroeder CE. Neuronal oscillations and multisensory interaction in primary auditory cortex. Neuron 2007, 53: 279–292.
5. Koelsch S, Skouras S, Lohmann G. The auditory cortex hosts network nodes influential for emotion processing: An fMRI study on music-evoked fear and joy. PLoS One 2018, 13: e0190057.
6. Li JC, Liao X, Zhang JX, Wang M, Yang N, Zhang J, *et al*. Primary auditory cortex is required for anticipatory motor response. Cereb Cortex 2017, 27: 3254–3271.
7. Francis NA, Winkowski DE, Sheikhattar A, Armengol K, Babadi B, Kanold PO. Small networks encode decision-making in primary auditory cortex. Neuron 2018, 97: 885-897.e6.
8. King AJ, Teki S, Willmore BDB. Recent advances in understanding the auditory cortex. F1000Res 2018, 7: F1000 Faculty Rev 1555.
9. Kimura A, Donishi T, Okamoto K, Tamai Y. Topography of projections from the primary and non-primary auditory cortical areas to the medial geniculate body and thalamic reticular nucleus in the rat. Neuroscience 2005, 135: 1325–1342.
10. Zingg B, Hintiryan H, Gou L, Song MY, Bay M, Bienkowski MS, *et al*. Neural networks of the mouse neocortex. Cell 2014, 156: 1096–1111.
11. Zhang ZJ, Zhang HR, Wen PJ, Zhu XT, Wang L, Liu Q, *et al*. Whole-brain mapping of the inputs and outputs of the medial part of the olfactory tubercle. Front Neural Circuits 2017, 11: 52.
12. Nelson A, Schneider DM, Takatoh J, Sakurai K, Wang F, Mooney R. A circuit for motor cortical modulation of auditory cortical activity. J Neurosci 2013, 33: 14342–14353.
13. Morrill RJ, Hasenstaub AR. Visual information present in infragranular layers of mouse auditory cortex. J Neurosci 2018, 38: 2854–2862.
14. Ji XY, Zingg B, Mesik L, Xiao ZJ, Zhang LI, Tao HW. Thalamocortical innervation pattern in mouse auditory and visual cortex: Laminar and cell-type specificity. Cereb Cortex 2016, 26: 2612–2625.
15. Cai DQ, Yue Y, Su X, Liu MM, Wang YW, You L, *et al*. Distinct anatomical connectivity patterns differentiate subdivisions of the nonlemniscal auditory thalamus in mice. Cereb Cortex 2019, 29: 2437–2454.
16. Rock C, Zurita H, Wilson C, Apicella AJ. An inhibitory corticostriatal pathway. Elife 2016, 5: e15890.
17. Chen CG, Cheng MX, Ito T, Song S. Neuronal organization in the inferior colliculus revisited with cell-type-dependent monosynaptic tracing. J Neurosci 2018, 38: 3318–3332.
18. Douglas RJ, Martin KA. Neuronal circuits of the neocortex. Annu Rev Neurosci 2004, 27: 419–451.
19. Wall NR, De La Parra M, Sorokin JM, Taniguchi H, Huang ZJ, Callaway EM. Brain-wide maps of synaptic input to cortical interneurons. J Neurosci 2016, 36: 4000–4009.
20. Holmgren C, Harkany T, Svennenfors B, Zilberter Y. Pyramidal cell communication within local networks in layer 2/3 of rat neocortex. J Physiol 2003, 551: 139–153.
21. Atencio CA, Schreiner CE. Spectrotemporal processing differences between auditory cortical fast-spiking and regular-spiking neurons. J Neurosci 2008, 28: 3897–3910.
22. Cai DQ, Han RR, Liu MM, Xie FH, You L, Zheng Y, *et al*. A critical role of inhibition in temporal processing maturation in the primary auditory cortex. Cereb Cortex 2018, 28: 1610–1624.
23. da Costa NM, Martin KA, Sägesser FD. A weighted graph of the projections to mouse auditory cortex. bioRxiv 2017: 228726. https://doi.org/10.1101/228726.
24. Oh SW, Harris JA, Ng L, Winslow B, Cain N, Mihalas S, *et al*. A mesoscale connectome of the mouse brain. Nature 2014, 508: 207–214.
25. Gong H, Xu DL, Yuan J, Li XN, Guo CD, Peng J, *et al*. High-throughput dual-colour precision imaging for brain-wide connectome with cytoarchitectonic landmarks at the cellular level. Nat Commun 2016, 7: 12142.
26. Sun P, Jin S, Tao S, Wang J, Li A, Li N, *et al*. Highly efficient and super-bright neurocircuit tracing using vector mixing-based virus cocktail. bioRxiv 2020: 705772. https://doi.org/10.1101/705772.
27. Sun QT, Li XN, Ren M, Zhao MT, Zhong QY, Ren YQ, *et al*. A whole-brain map of long-range inputs to GABAergic interneurons in the mouse medial prefrontal cortex. Nat Neurosci 2019, 22: 1357–1370.

28. Regan KS. Book review: Allen reference atlas. A digital color brain atlas of the C57BL/6J male mouse. Vet Pathol 2008, 45: 724–725.
29. Li XN, Yu B, Sun QT, Zhang YL, Ren M, Zhang XY, *et al*. Generation of a whole-brain atlas for the cholinergic system and mesoscopic projectome analysis of basal forebrain cholinergic neurons. Proc Natl Acad Sci USA 2018, 115: 415–420.
30. Wang QX, Ding SL, Li Y, Royall J, Feng D, Lesnar P, *et al*. The Allen mouse brain common coordinate framework: A 3D reference atlas. Cell 2020, 181: 936-953.e20.
31. Ni H, Tan CZ, Feng Z, Chen SB, Zhang ZT, Li WW, *et al*. A robust image registration interface for large volume brain atlas. Sci Rep 2020, 10: 2139.
32. Quan TW, Zheng T, Yang ZQ, Ding WX, Li SW, Li J, *et al*. NeuroGPS: automated localization of neurons for brain circuits using L1 minimization model. Sci Rep 2013, 3: 1414.
33. Li YX, Gong H, Yang XQ, Yuan J, Jiang T, Li XN, *et al*. TDat: an efficient platform for processing petabyte-scale whole-brain volumetric images. Front Neural Circuits 2017, 11: 51.
34. Otsu N. A threshold selection method from gray-level histograms. IEEE Trans Syst Man Cybern 1979, 9: 62–66.
35. Barone P, Batardiere A, Knoblauch K, Kennedy H. Laminar distribution of neurons in extrastriate areas projecting to visual areas V1 and V4 correlates with the hierarchical rank and indicates the operation of a distance rule. J Neurosci 2000, 20: 3263–3281.
36. Budinger E, Kanold PO. Auditory Cortex Circuits, The Mammalian Pathways: Synaptic organization and microcircuits. In Oliver DL, Cant NB, Fay RR, Popper AN (eds) Handbook of Auditory Research Series, Springer, 2018, vol. 65, pp. 200.
37. Budinger E, Scheich H. Anatomical connections suitable for the direct processing of neuronal information of different modalities via the rodent primary auditory cortex. Hear Res 2009, 258: 16–27.
38. Hu B, Senatorov V, Mooney D. Lemniscal and non-lemniscal synaptic transmission in rat auditory thalamus. J Physiol 1994, 479: 217–231.
39. Ährlund-Richter S, Xuan Y, van Lunteren JA, Kim H, Ortiz C, Dorocic IP, *et al*. A whole-brain atlas of monosynaptic input targeting four different cell types in the medial prefrontal cortex of the mouse. Nat Neurosci 2019, 22: 657–668.
40. Gehrlach DA, Weiand C, Gaitanos TN, Cho E, Klein AS, Hennrich AA, *et al*. A whole-brain connectivity map of mouse insular cortex. Elife 2020, 9: e55585.
41. Duan ZN, Li AA, Gong H, Li XN. A whole-brain map of long-range inputs to GABAergic interneurons in the mouse caudal forelimb area. Neurosci Bull 2020, 36: 493–505.
42. Harris JA, Mihalas S, Hirokawa KE, Whitesell JD, Choi H, Bernard A, *et al*. Hierarchical organization of cortical and thalamic connectivity. Nature 2019, 575: 195–202.
43. Horie M, Tsukano H, Hishida R, Takebayashi H, Shibuki K. Dual compartments of the ventral division of the medial geniculate body projecting to the core region of the auditory cortex in C57BL/6 mice. Neurosci Res 2013, 76: 207–212.
44. Winer JA, Sally SL, Larue DT, Kelly JB. Origins of medial geniculate body projections to physiologically defined zones of rat primary auditory cortex. Hear Res 1999, 130: 42–61.
45. McDonald CT, Burkhalter A. Organization of long-range inhibitory connections with rat visual cortex. J Neurosci 1993, 13: 768–781.
46. Tomioka R, Okamoto K, Furuta T, Fujiyama F, Iwasato T, Yanagawa Y, *et al*. Demonstration of long-range GABAergic connections distributed throughout the mouse neocortex. Eur J Neurosci 2005, 21: 1587–1600.
47. Higo S, Akashi K, Sakimura K, Tamamaki N. Subtypes of GABAergic neurons project axons in the neocortex. Front Neuroanat 2009, 3: 25.
48. Knowland D, Lilascharoen V, Pacia CP, Shin S, Wang EH, Lim BK. Distinct ventral pallidal neural populations mediate separate symptoms of depression. Cell 2017, 170: 284-297.e18.
49. Kudo M, Niimi K. Ascending projections of the inferior colliculus in the cat: An autoradiographic study. J Comp Neurol 1980, 191: 545–556.
50. Swanson LW. Brain maps 4.0-Structure of the rat brain: An open access atlas with global nervous system nomenclature ontology and flatmaps. J Comp Neurol 2018, 526: 935–943.